

X-ray Irradiation of the Giant Planet Orbiting the T Tauri Star TAP 26

STEPHEN L. SKINNER¹ AND MANUEL GÜDEL²

¹*Center for Astrophysics and Space Astronomy (CASA), Univ. of Colorado, Boulder, CO, USA 80309-0389*

²*Dept. of Astrophysics, Univ. of Vienna, Türkenschanzstr. 17, A-1180 Vienna, Austria*

Submitted to ApJ

ABSTRACT

We present new Chandra X-ray observations of TAP 26, a ≈ 17 Myr old magnetically-active weak-lined T Tauri star that has been reported to host a massive planet in a ≈ 10.8 day orbit. At a separation of $a = 0.097$ AU the planet will be exposed to intense X-ray and UV radiation from the star. The first observation caught the star in a state of elevated X-ray emission with variability on a timescale of a few hours and an X-ray temperature $kT_x \approx 2 - 4$ keV. Two subsequent observations 5-10 days later showed slow variability and a lower X-ray flux and temperature ($kT_x \approx 1$ keV). We characterize the X-ray emission and estimate the X-ray ionization and heating rates that will need to be incorporated into realistic models of the planet's atmosphere.

Keywords: stars: individual (TAP 26) — stars: pre-main-sequence — X-rays: stars

1. INTRODUCTION

Observational studies of planet-hosting T Tauri stars (TTS) provide crucial information on the environments in which planets form around solar-like stars. At ages of a few Myr the high-energy X-ray and UV (XUV) emission from TTS can be a thousand times more luminous than their main-sequence descendants. This intense XUV radiation heats and ionizes gas in the inner disk and in the atmospheres of close-in exoplanets, influencing atmospheric temperature, chemistry, and mass loss. Thus the effects of XUV radiation must be considered in models of exoplanet formation, evolution, and even the survival of close-in planets.

Most exoplanet discoveries so far have been around old mature host stars (ages $\gtrsim 1$ Gyr) but ongoing searches are now revealing exoplanets around a few young TTS. The discovery of exoplanets orbiting TTS a few million years old are important because they provide a snapshot of conditions in the planet-forming environment during the early stages of planet formation. One of the most compelling examples so far is the weak-lined TTS PDS 70 for which two formative giant planets have been directly imaged at deprojected separations of $\approx 20 - 40$ AU from the star (Keppler et al. 2018, 2019; Haffert et al. 2019). But at this separation the planets will be little affected by stellar XUV radiation (Skinner & Audard 2022). In contrast, TTS such as TAP 26 discussed here represent the opposite extreme where the exoplanet orbits very close to the host star, thus exposing it directly to

the intense XUV radiation field. The X-ray emitting weak-lined TTS V830 Tau may also harbor a close-in massive planet and its properties are summarized below (Sec. 4.5).

A Massive Planet Orbiting TAP 26. Periodic radial velocity variations in the weak-lined TTS TAP 26 (= V1069 Tau) have been attributed to a giant planet V1069 Tau b (also called TAP 26 b) orbiting at a close separation $a = 0.097$ au (Yu et al. 2017; hereafter Yu17), about four times smaller than Mercury’s semi-major axis. The near-circular orbit has a period of 9 - 11 d with a most likely value $P_{orb} = 10.79$ d. The planet has a minimum mass $M_p \sin i = 1.66 M_J$ where M_J is Jupiter’s mass. If the planet’s orbital and equatorial planes are aligned at $i \approx 55^\circ$ then $M_p = 2.03 \pm 0.46 M_J$ (Yu17).

The host star TAP 26 is a K7e type weak-lined TTS in the Taurus star-forming region at a *Gaia* DR3 parallax distance $d = 121.6 \pm 0.2$ pc which we adopt herein. It is viewed through low extinction $A_V = 0.25\text{-}0.43$ mag (Herczeg & Hillenbrand 2014). Stellar properties are given in Yu17 who assumed a distance of 147 pc and derived a mass $M_* = 1.04 \pm 0.1 M_\odot$, stellar luminosity $\log(L_*/L_\odot) = -0.25 \pm 0.10$, and an age of ≈ 17 Myr. The star is a rapid rotator with $P_{rot} = 0.7135$ d (Grankin 2013) and is magnetically active (Yu17).

TAP 26 is a prominent X-ray source and has been detected by ROSAT and the Einstein Observatory. Being a ~ 17 Myr old weak-lined TTS its disk has largely dissipated and the exoplanet is directly exposed to intense high-energy XUV stellar radiation. The XUV radiation is expected to heat the planet’s atmosphere to a maximum temperature of $\sim 10^4$ K, well above typical equilibrium temperatures of a few hundred K to ~ 2500 K (Fortney, Dawson, & Komacek 2021). As such, the TAP 26 system provides an excellent laboratory to study a “hot Jupiter” in a harsh XUV environment that will contribute to atmospheric heating and photoevaporation.

TAP 26 is one of the youngest T Tauri stars known so far to host a hot Jupiter. Since the mass of TAP 26 is nearly identical to the Sun it is a benchmark laboratory for constraining giant planet formation around solar-like stars. The question of how Jupiter-mass planets end up in orbits so close to their host stars is much debated and both *in situ* and migration models have been proposed (see reviews by Dawson & Johnson 2018; Fortney et al. 2021). TAP 26 b migration scenarios were considered by Yu17.

2. X-RAY OBSERVATIONS

TAP 26 was detected in X-rays in the *ROSAT* All-Sky Survey (Neuhäuser et al. 1995) and in a *ROSAT* PSPC pointed observation (source 1WGA J0418.8+1723). It was also detected in two Einstein Imaging Proportional Counter (IPC) observations (Feigelson et al. 1987) with a reported flux $F_x(0.2\text{-}4 \text{ keV}) = (3.9 - 4.6) \times 10^{-13} \text{ ergs cm}^{-2} \text{ s}^{-1}$.

We observed TAP 26 with Chandra in December 2021 using the Advanced CCD Imaging Spectrometer (ACIS-S), as summarized in Table 1. The 60 ks observation was obtained in three segments over a timespan of ≈ 11 days as a result of Chandra’s operational constraints. Data were reduced using Chandra Interactive Analysis of Observations (CIAO vers. 4.14) software in combination with CALDB vers. 4.9.8 calibration data¹. Separate spectra and X-ray light curves were generated for each observation using events within a circular region of radius $2''$ centered on the source peak. X-ray spectra and associated response matrix files (rmf) and auxiliary response files (arf) were extracted using CIAO *specextract*. Energy-filtered light curves were produced using CIAO *dmextract* in broad (0.3-8 keV), soft (0.3-2 keV), and hard (2-8 keV) bands. CIAO *glvary* was used to check for source

¹ For more information on CIAO and CALDB see <https://cxc.cfa.harvard.edu>.

Table 1. Summary of TAP 26 Chandra Observations

Parameter	Observation		
ObsId	25693	25124	26225
Start Date (2021)/Time (TT)	Dec. 1/07:38	Dec. 6/23:52	Dec. 11/13:40
Stop Date (2021)/Time (TT)	Dec. 1/13:39	Dec. 7/08:49	Dec. 11/17:02
Start MJD (d)	59549.318	59554.995	59559.569
Elapsed Time (ks)	21.665	32.211	12.078
Livetime (ks) ^b	17.989	27.227	9.456
ϕ_{rot} ^c	0.0 - 0.35	0.96 - 0.31	0.37 - 0.57

^aData were obtained using ACIS-S in faint timed event mode, a frame time of 0.6 s, and the source positioned on CCD S3. The X-ray centroid position of TAP 26 from is (J2000) R.A. = $04^{\text{h}}18^{\text{m}}51^{\text{s}}.72$, decl. = $+17^{\circ}23'15''.6$. The *Gaia* DR3 position is R.A. = $04^{\text{h}}18^{\text{m}}51^{\text{s}}.71$, decl. = $+17^{\circ}23'16''.4$.

^bLivetime is the time during which data were being collected and excludes operational and instrumental overheads such as CCD readout times.

^cRotational phase is computed assuming $P_{rot} = 0.7135$ d (Yu et al. 2017) and $\phi_{rot} = 0$ is arbitrarily defined to be the start of ObsId 25693.

variability and compute the probability of variability P_{var} . Background and pileup were negligible. Spectra were analyzed using XSPEC vers. 12.10.1.

3. RESULTS

3.1. X-ray Light Curves and Spectra

TAP 26 was detected as a variable X-ray source as summarized in Table 2. The X-ray light curves are shown in Figure 1. Hereafter, we refer to ObsId 25693 as high-state and ObsIds 25124 and 26225 as low-state since the count rate and flux were twice as high in ObsId 25693.

An abrupt rise and fall in broad-band count rate is clearly visible in the broad-band ObsId 25693 light curve and the variability probability is $P_{var} = 0.99$. A slow decline in broad-band count rate also occurred in ObsId 25124 with the mean rate in the second half of the observation being $\approx 25\%$ less than the first half and $P_{var} = 0.87$. No significant variability was detected in the last and shorter observation ObsId 26225 ($P_{var} = 0.12$). The soft-band (0.3-2 keV) emission dominates the light curves in all observations. But in ObsId 25693 the hardness ratio and hard-band (2-8 keV) count rate of $8.5 \pm 0.7 \text{ c ks}^{-1}$ were higher than the other two observations. This reflects the higher plasma temperature that was measured in ObsId 25693 (Sec. 4.2). ObsId 25124 was obtained about five days after ObsId 25693 and at nearly the same rotational phase, but the broad-band count rate and flux were a factor of two lower. Thus the elevated emission detected in ObsId 25693 is evidently not tied to the star's rotational phase (Table 1).

Spectra were fitted in XSPEC with absorbed (*tbabs*) one-temperature (1T) or two-temperature (2T) *apec* and *vapec* (variable abundances) thin plasma models. The absorption is low and not well-constrained by the data so N_H was held fixed during fitting at $N_H = 6.65 \times 10^{20} \text{ cm}^{-2}$ corresponding to $A_V \approx 0.35 \text{ mag}$ and the adopted conversion $N_H (\text{cm}^{-2}) = 1.9 \pm 0.3 \times 10^{21} \cdot A_V$ (Gorenstein 1975; Vuong et al. 2003). The spectra obtained in ObsIds 25124 and 26225 when the count rate was lower (low-state) are nearly identical and were thus fitted simultaneously in XSPEC to reduce the uncertainties in best-fit parameters. A simple isothermal 1T *apec* model allowing the metallicity Z to vary provides a very good fit of the low-state spectra and converges to $kT \approx 1 \text{ keV}$ and a low metallicity $Z = 0.15 \pm 0.04 Z_\odot$ (Table 2). Since X-rays from weak-lined TTS are thought to arise in hot magnetically-confined plasma analogous to the solar corona, this metallicity reflects coronal abundances, not photospheric.

As shown in Figure 2, the high-state spectrum (ObsId 25693) shows strong emission in the 0.9 - 1.2 keV range that is also visible but weaker in the low-state spectrum (ObsId 25124). Emission in this energy range is attributable to the Ne IX triplet ($E_{lab} = 0.92 \text{ keV}$, maximum line power at $\log T_{max} = 6.6 \text{ K}$), Ne X ($E_{lab} = 1.02 \text{ and } 1.21 \text{ keV}$, $\log T_{max} = 6.8 \text{ K}$), and a possible contribution from multiple closely-space Fe lines near 1 keV. The Si XIII triplet (1.86 keV, $\log T_{max} = 7.0 \text{ K}$) is also clearly present in the high-state spectrum. The high-state spectrum required a two-temperature model (2T *vapec*) to obtain a satisfactory fit and it is improved by allowing the abundances of Ne and Fe to vary rather than just varying the metallicity Z . While varying the Ne abundance it was constrained to be equal for both temperature components and similarly for Fe. The 2T *vapec* fits converge to a low iron abundance $\text{Fe} = 0.15 \pm 0.12$ times solar but a Ne abundance above solar is required to reproduce the strong Ne line emission (Table 2). The plasma was hotter in high-state with a characteristic temperature weighted by the emission measure (EM) contributions of the cool and hot components $kT_{wgt} = 1.6 \text{ keV}$ compared to $kT = 1.0 \text{ keV}$ in low-state. The X-ray luminosity was about 2.5 times higher in high-state.

Table 2. Summary of TAP 26 X-ray Properties (Chandra ACIS-S)

ObsId (state)	Rate (c ks ⁻¹)	Counts (c)	Hardness Ratio	E ₅₀ (keV)	kT (keV)	F _{x,abs} (ergs cm ⁻² s ⁻¹)	log L _x (ergs s ⁻¹)
25693 (high)	44.4(v)	798	0.26	1.49	1.62 ^b	6.84±0.35e-13 ^b	30.20 ^b
25124 (low)	22.0(v)	598	0.17	1.33	1.02 ^c	2.77±0.10e-13 ^c	29.80 ^c
26225 (low)	21.5	203	0.16	1.28	1.02 ^c	2.77±0.81e-13 ^c	29.80 ^c
Time Partitioned Data ^d							
25693 (pre-flare)	37.9	248	0.28	1.56	2.82	4.84±0.69e-13	30.03
25693 (flare)	56.1	420	0.26	1.49	2.03	6.69±0.53e-13	30.17
25693 (post-flare)	32.9	130	0.26	1.31	0.96	3.21±0.26e-13	29.86

^a Notes: Mean count rate (Rate = counts/livetime) where (v) denotes the rate was variable, counts, hardness ratio = counts(2-8 keV)/counts(0.3-8 keV), median event energy (E₅₀), plasma temperature (kT) in energy units weighted by emission measure contribution for 2T models, absorbed X-ray flux (F_{x,abs}±1σ), and unabsorbed X-ray luminosity (L_x, at d = 121.6 pc). Tabulated values were computed using events in the 0.3-8 keV range.

^bBased on a spectral fit of the ObsId 25693 spectrum rebinned to a minimum of 10 counts per bin using an absorbed 2T *vap*ec model of the form N_H^{*}(kT₁ + kT₂) with absorption (XSPEC *tbabs*) held fixed at N_H = 6.65e20 cm⁻² and allowing the abundances of Ne and Fe to vary (Ne = 1.80±0.59, Fe = 0.15±0.12 × solar; referenced to the solar abundances of Anders & Grevesse 1989). kT is the emission-measure (EM) weighted value of the two temperature components (kT₁ = 0.38±0.04, kT₂ = 2.91±0.47 keV, EM₁/EM₂ = 1.05, χ²/dof = 59.2/59 = 1.00, 1σ errors).

^cBased on a simultaneous fit of the spectra for ObsIds 25124 and 26225 rebinned to a minimum of 10 counts per bin using an absorbed 1T *ap*ec plasma model of the form N_H^{*}(kT) with absorption (XSPEC *tbabs*) held fixed at N_H = 6.65e20 cm⁻², kT = 1.02±0.04 keV, best-fit metallicity Z = 0.15±0.04 Z_⊙, χ²/dof = 60.9/66 = 0.92, 1σ errors).

^dBased on fits of the ObsId 25693 spectra for the pre-flare (livetime 6551 s), flare (7488 s), and post-flare (3950 s) segments (Sec. 4.1). The value of P_{var} was not computed for individual time segments.

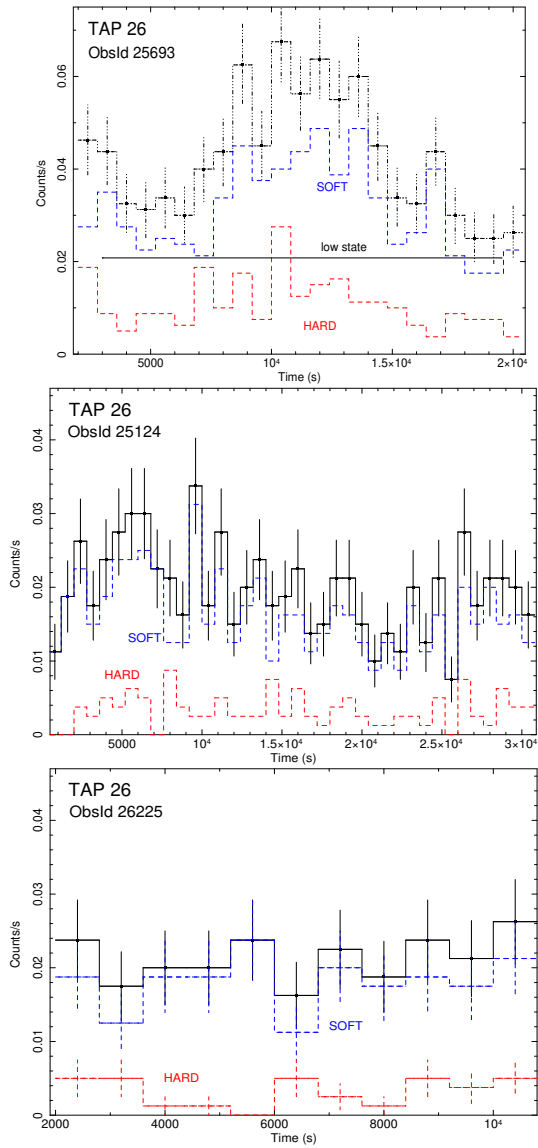


Figure 1. *Chandra* ACIS-S light curves of TAP 26 binned at 800 s intervals in broad 0.3-8 keV (black), soft 0.3-2 keV (blue), and hard 2-8 keV (red) energy bands. Times are relative to start of each *Chandra* observation (Table 2). For comparison, the solid horizontal solid line in the high-state variable light curve of ObsId 25693 (top) shows the mean count rate (0.3-8 keV) during the short low-state observation ObsId 26225 (bottom).

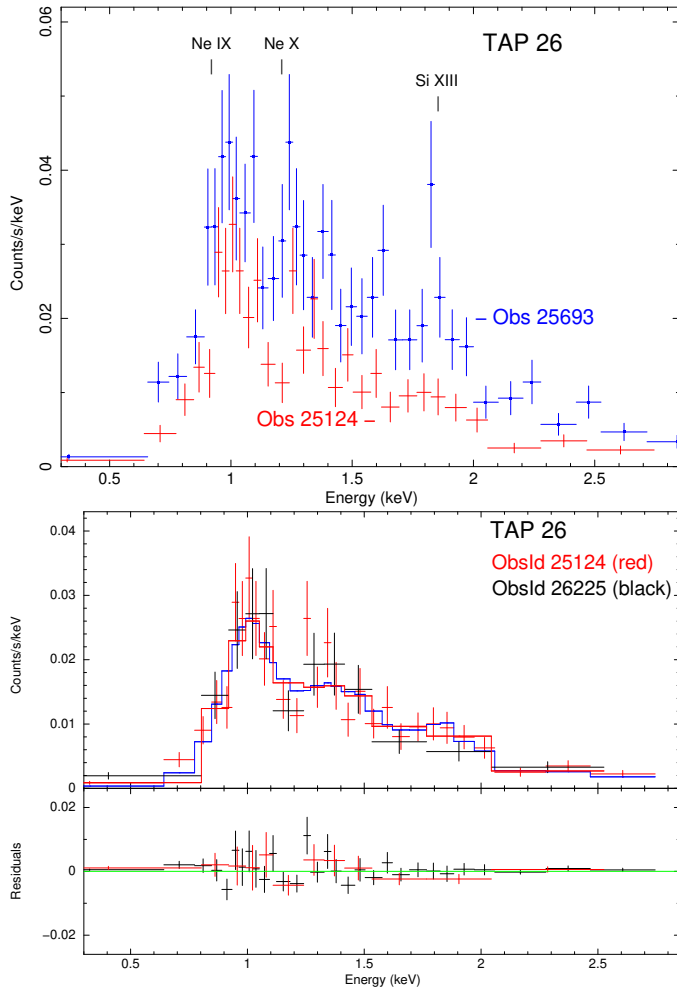


Figure 2. Chandra ACIS-S spectra of TAP 26, rebinned for display. Error bars are 1σ . Top: Overlay of high-state (ObsId 25693, blue) and low-state (ObsId 25124, red). A few candidate emission lines (or blends) are identified. Bottom: Overlay of TAP 26 low-state spectra for ObsId 25124 (red, 598 cts) and 26225 (black, 203 cts). The blue solid line is a simultaneous fit of the two spectra using the 1T *apec* model ($kT = 1.02$ keV) whose best-fit parameters are given in Table 2 notes. Fit residuals are shown at bottom.

4. DISCUSSION

4.1. X-ray Variability

A comparison of the low and high-state measurements (Table 2) shows that the flux and X-ray luminosity of TAP 26 varied by a factor of ≈ 2.5 within a five day interval. The high-state light curve for ObsId 25693 reveals short-term variability on a timescale of a few hours. An exponential fit of the declining X-ray light curve during the last half of ObsId 25693 after the count rate peaked gives an e-folding timescale of ≈ 9 ks. In addition ObsId 25124 reveals a slow decline in count rate over ≈ 8 hours. For a comparison on a timescale of decades with the Einstein IPC we measured the Chandra fluxes in the IPC energy range and obtained $F_x(0.2-4 \text{ keV}) = 2.72 \pm 0.14 \times 10^{-13}$ (low-state) and $6.23 \pm 0.36 \times 10^{-13}$ (high-state) $\text{ergs cm}^{-2} \text{ s}^{-1}$. This range encompasses the IPC flux (Feigelson et al. 1987) of $F_x(0.2-4 \text{ keV}) = (3.9-4.6) \times 10^{-13} \text{ ergs cm}^{-2} \text{ s}^{-1}$.

To investigate in more detail the changes in X-ray emission that occurred during ObsId 25693 we extracted time-partioned events and spectra from the first ≈ 7 ks when the light curve was nearly steady (pre-flare), the middle ≈ 8 ks when the count rate rose and declined (flare), and the last ≈ 4 ks (post-flare) when the count rate had declined to a value nearly the same as at the start of the observation. We use the term “flare” here in a general sense to denote the rise and fall in count rate over a time interval of about two hours, even though the rise was not impulsive. Spectra for each time segment were fitted and the results are summarized in Table 2. Since the time-partioned spectra contain fewer counts than the total spectrum, uncertainties in best-fit parameters are larger. Even so, the three segments show clear differences in temperature and flux.

At the start of ObsId 25693 the count rate, temperature, and flux were already elevated above the low-state values observed in the two subsequent observations. A 2T *vapex* fit of the pre-flare spectrum gives a hot component temperature $kT_2 = 5.5$ (3.4 - 12.7, 1σ range) keV with $\approx 47\%$ of the EM in the hot component. The count rate and L_x peaked during the flare and a 2T *vapex* fit yields $kT_2 = 3.0$ (2.4 - 4.3) keV with $\approx 61\%$ of the EM in the hot component and $\log L_x = 30.17$ ergs s^{-1} . Even though the best-fit value of kT_2 during the flare segment was somewhat lower than during pre-flare, the uncertainty ranges are large enough to allow overlap. During the last ≈ 4 ks (post-flare) the emission had fallen off to values only marginally higher than in low-state with an isothermal 1T plasma model giving $kT = 1.0$ (0.9 - 1.1) keV. The above results show that the event recorded in ObsId 25693 was already in progress when the observation began but the emission had declined to near low-state levels by the end of the observation. The duration of the elevated emission (pre-flare+flare) was at least ≈ 15 ks.

Since the elevated flux and temperature were not detected five days later at the same rotational phase in ObsId 25124, the high emission state is not consistent with a long-lived active region on the star that might have been caught by chance rotating across the line-of-sight. But the observed X-ray variability in ObsId 25693 is consistent with a modest X-ray flare. The analysis of T Tauri star X-ray flares detected in a XMM-Newton X-ray of the Taurus Molecular Cloud (TMC) by Franciosini et al. (2007) revealed peak luminosities $\log L_x \geq 31$ ergs s^{-1} , high plasma temperatures ≥ 5 keV (60 MK), rise times of $\approx 1 - 35$ ks, and decay timescales of $\approx 2 - 45$ ks. The TAP 26 variability in Obs 25693 fits within these ranges. Even so, the additional detection of slow low-amplitude variability in ObsId 25124 when the emission was less luminous justifies further time monitoring to determine whether the variability is modulated on longer timescales such as the planet’s ≈ 10.8 day orbital period.

A previous XMM-Newton X-ray study of TTS in the TMC by Telleschi et al. (2007) derived relations between L_x and stellar parameters. For weak-lined TTS they found a mean fractional X-ray luminosity $\log(L_x/L_*) = -3.36 \pm 0.07$. To compare this with TAP 26 we scale its value $L_*/L_\odot = 0.56$ (0.45 - 0.71) as determined by Yu17 using $d = 147$ pc down to the *Gaia* DR3 distance of 121.6 pc which gives $L_*/L_\odot = 0.38$ (0.31 - 0.48). The observed TAP 26 X-ray luminosities (Table 2) then give $\log(L_x/L_*) = -3.36 \pm 0.10$ (low-state) and -2.96 ± 0.10 (high-state). The low-state value thus agrees well with the mean for weak-lined TTS in the TMC sample. But the high state value lies at the high end of the range observed for weak-lined TTS with masses $> 0.7 M_\odot$ and is atypical (Fig. 8-right of Telleschi et al. 2007). Thus, the low-state value $\log L_x(0.3-8 \text{ keV}) = 29.8 \text{ ergs s}^{-1}$ probably represents the typical X-ray luminosity of TAP 26.

4.2. X-ray Ionization and Heating

Using the L_x values in Table 2 the unattenuated X-ray flux at the planet's distance of 0.097 AU is $F_{x,unatten} = (2.4 - 6.0) \times 10^4 \text{ ergs cm}^{-2} \text{ s}^{-1}$. This is $\sim 10^6$ times greater than the Sun's flux at Jupiter assuming a nominal solar X-ray luminosity $\log L_{x,\odot} = 27.3 \text{ ergs s}^{-1}$.

We estimate the X-ray ionization and heating rates at the TAP 26 planet's separation using the procedure given for V830 Tau in Skinner & Güdel (2021) and further details can be found therein. The X-ray ionization rate at a distance r from the star for a thermal plasma at X-ray temperature kT_x is (Shang et al. 2002)

$$\zeta(r) \approx \zeta_x \left[\frac{r}{R_x} \right]^{-2} \left[\frac{kT_x}{\epsilon_{ion}} \right] I(\tau_x) \quad (\text{s}^{-1} \text{ per H nucleus}). \quad (1)$$

where ζ_x is the primary ionization rate (eq. [2]), R_x is the distance of the X-ray source above the star, $\epsilon_{ion} \approx 37 \text{ eV}$ is the energy to create an ion pair, and $I(\tau_x)$ is an X-ray attenuation factor evaluated at optical depth τ_x .

For coronal X-ray emission R_x corresponds to at most a few stellar radii and we simply use $R_x \approx R_* = 1.17 R_\odot$ (Yu17) for TAP 26, so the computed value of $\zeta(r)$ will be a lower limit. The results of Shang et al. (2002) include attenuation by a disk wind in the expression for $I(\tau_x)$ but this effect is negligible for a weak-lined TTS like TAP 26 where the disk has dissipated so we adopt the approximate relation $I(\tau_x) \approx e^{-\tau_x}$. The height z in the planet's atmosphere corresponding to a given value τ_x depends on the atmospheric model which explicitly specifies the number density of hydrogen nuclei versus height $n_H(z)$. Since the planet's properties are not yet characterized we do not adopt a specific planet atmospheric model. For a photon of energy E the equivalent neutral hydrogen column density along the line-of-sight from the star to the point in the planet's atmosphere at which $\tau_x = 1$ is simply $N_{H,\tau_x=1} = 1/\sigma(E)$. The X-ray photoelectric absorption cross-section declines rapidly with photon energy as $\sigma(E) = \sigma_0(E/1 \text{ keV})^{-p} \text{ cm}^{-2}$ where $\sigma_0 = 2.27 \times 10^{-22} \text{ cm}^2$ and $p = 2.485$ for solar abundances but the value of p is abundance dependent (Morrison & McCammon 1983; Igea & Glassgold 1999; Shang et al. 2002). Thus lower energy X-rays are more heavily absorbed in the planet's outer atmosphere, all other factors being equal. Scattering effects are negligible at energies below a few keV of interest here (Bruderer et al. 2009).

The total X-ray ionization rate given by eq. (1) above accounts for multiple secondary ionizations resulting from the primary photoelectron ionization rate

$$\zeta_x = 1.13 \times 10^{-8} \left[\frac{L_x}{10^{30} \text{ erg s}^{-1}} \right] \left[\frac{kT_x}{\text{keV}} \right]^{-(p+1)} \left[\frac{R_x}{10^{12} \text{ cm}} \right]^{-2} \quad (\text{s}^{-1}). \quad (2)$$

The X-ray heating rate per unit volume is

$$\Gamma_x = \epsilon_x \zeta n_H Q \quad (3)$$

where $0 < \epsilon_x < 1$ is the fractional X-ray heating efficiency, $Q \approx 20$ eV is the heating rate per ionization and n_H is the number density of hydrogen nuclei in the planet's atmosphere at the height z corresponding to the X-ray optical depth at which ζ is computed (eq. 1). Rewriting the above equation in normalized form gives

$$\Gamma_x = 3.2 \times 10^{-9} \epsilon_x \left[\frac{\zeta}{10^{-8} \text{ s}^{-1} \text{ H}^{-1}} \right] \left[\frac{n_H}{10^{10} \text{ cm}^{-3}} \right] \left[\frac{Q}{20 \text{ eV}} \right] \quad (\text{ergs cm}^{-3} \text{ s}^{-1}). \quad (4)$$

Table 3 summarizes the ionization and heating rates for TAP 26 in low and high X-ray emission states evaluated at $\tau_x = 1$. Since we do not invoke a specific planet atmosphere model the value of n_H used to compute Γ_x in Table 3 is left unspecified. The high state heating rate in Table 3 is evaluated using the weighted plasma temperature and the combined L_x of the cool and hot plasma components, as well as separately for the contributions of each temperature component. When the weighted temperature is used, the low and high state heating rates are nearly the same. But when each temperature component is treated separately the cool plasma dominates the heating. This clearly shows that the computed heating rate is sensitive to the assumed plasma temperature, a consequence of the steep falloff in the primary photoionization rate ζ_x with increasing temperature (eq. [2]).

Table 3. X-ray Ionization and Heating Rates (TAP 26)

State	r	kT _x	log L _x	ζ _x	ζ(r)	N _H (τ _x =1)	Γ _x
	(au)	(keV)	(ergs s ⁻¹)	(s ⁻¹)	(s ⁻¹ H ⁻¹)	(cm ⁻²)	(ergs s ⁻¹ cm ⁻³ n _H ⁻¹)
Low ^a	0.0968	1.02	29.8	1.00e-06	3.2e-08	8.45e21	1.0e-18
High ^b	0.0968	1.62	30.2	0.50e-06	2.6e-08	1.21e22	8.3e-19
High ^c	0.0968	0.38 (kT ₁)	29.94	4.32e-05	51.4e-08	4.52e20	1.6e-17
High ^c	0.0968	2.9 (kT ₂)	29.85	2.96e-08	0.3e-08	6.21e22	8.6e-20

NOTE— The secondary ionization rate ζ (eq. [1]), primary ionization rate ζ_x (eq. [2]), and heating rate Γ_x (eq. [3]) are computed at τ_x = 1 using ε_x = 1, R_x = R_{*} = 1.17 R_☉, Q = 20 eV, and the assumed planet separation r = a = 0.0968 au. N_H(τ_x=1) = 1/σ(E₅₀) where E₅₀ is the median photon energy (Table 2). The number density n_H at height z in the planet’s atmosphere corresponding to τ_x=1 required to evaluate Γ_x depends on the adopted planet atmosphere model and has been left as a free parameter.

^aLow state values of kT_x and L_x are from the 1T *apec* fit of ObsIds 25124 and 26225 (Table 2).

^bHigh state values of kT_x (weighted) and L_x are from the 2T *vapex* fit of ObsId 25693 (Table 2),

^cHigh state values are evaluated separately for the cool (kT₁) and hot (kT₂) plasma components from the 2T *vapex* fit of ObsId 25693 (Table 2),

4.3. EUV Heating

The planet's outer atmosphere will also be ionized and heated by stellar EUV photons ($\lambda = 124 - 920 \text{ \AA}$, $E = 0.013 - 0.1 \text{ keV}$). The heating is mitigated by competing processes such as radiative cooling by the far-UV Ly α line at 1215.7 \AA (Salz et al. 2016). We apply to TAP 26 the same procedure as was used for V830 Tau (Skinner & Güdel 2021) to estimate the EUV heating rate. Taking $L_x \approx 10^{30} \text{ ergs s}^{-1}$ as a representative value for TAP 26 the heating rate for a monoenergetic EUV photon flux at energy E at the planet's separation 0.097 au is, by analogy with eq. [6] of Skinner & Güdel (2021)

$$\Gamma_{\text{EUV}} = 3.8 \times 10^4 \eta \left[\frac{L_{\text{EUV}}}{L_x} \right] \sigma(E) e^{-\tau_{\text{euv}}} n_{\text{H}} \quad (\text{ergs cm}^{-3} \text{ s}^{-1}). \quad (5)$$

In the above, $0 < \eta < 1$ is the fractional EUV heating efficiency and the EUV cross-section is approximated by $\sigma(E) = 6 \times 10^{-20} (E/100 \text{ eV})^{-p} \text{ (cm}^2)$ with $p = 2.485$ (Bruderer et al. 2009). As for X-rays n_{H} is the H number density at height z corresponding to τ_{euv} . At a characteristic EUV energy $E_0 = 60 \text{ eV}$ unit optical depth $\tau_{\text{euv}} = 1$ occurs at $N_{\text{H}} = 5 \times 10^{18} \text{ cm}^{-2}$, about 3 orders of magnitude less than $\tau_x = 1$ at 1 keV . Thus, X-ray photons will penetrate to deeper layers of the planet's atmosphere. Inserting values for $\sigma(E)$ at $E = 60 \text{ eV}$ and $\tau_{\text{euv}} = 1$ in the above expression and normalizing the H number density to a representative hot Jupiter value (Penz et al. 2008; Murray-Clay et al. 2009, hereafter MC09) gives at $a = 0.097 \text{ AU}$

$$\Gamma_{\text{EUV}} = 3 \times 10^{-5} \eta \left[\frac{L_{\text{EUV}}}{L_x} \right] \left[\frac{n_{\text{H}}}{10^{10} \text{ cm}^{-3}} \right] \quad (\text{ergs cm}^{-3} \text{ s}^{-1}). \quad (6)$$

Heating efficiencies $\eta \approx 0.1 - 0.6$ have been used in theoretical studies (e.g. Penz et al. 2008; Shaikhislamov et al. 2014). L_{EUV} is generally not measurable from direct observations due to interstellar absorption but the approximation $L_{\text{EUV}} \approx L_x$ is sometimes adopted (e.g. Ribas et al. 2005; Owen & Jackson 2012). The evolutionary tracks derived by Tu et al. (2015) predict L_{EUV} and L_x as a function of age and an assumed stellar rotation rate at an age of 1 Myr . At an age of $\sim 17 \text{ Myr}$ the predicted values of L_{EUV} and L_x are similar to within a factor of a few.

4.4. Implications of XUV Irradiation of the Planet's Atmosphere

Although the planet's orbital separation and mass have been estimated its radius and atmospheric properties are unknown. In general, the atmospheres of hot Jupiters are not yet well-characterized so any discussion of XUV effects is subject to uncertainties in the adopted atmospheric model. Given our lack of knowledge of the atmospheric properties of TAP 26 b, detailed modeling is not yet warranted but some insight can be obtained based on previous studies of other hot Jupiters.

Hot Jupiters at close separation from TTS will experience photoevaporative mass loss. Since TTS are generally strong XUV sources, several studies have concluded that the planet's mass-loss rate should be determined using numerical hydrodynamic models (e.g. Yelle 2004; Penz et al. 2008; MC09; Salz et al. 2016). But other studies using analytic energy-limited approach predict mass loss rates that are not much different than obtained using hydrodynamic models (e.g. Shaikhislamov et al. 2014).

Hydrodynamic models assume a steady spherical wind similar to that of the solar wind developed by Parker (1958; 1965), except externally heated (ignoring any internal heating such as may arise from tidal dissipation). The mass loss rate as a function of radial distance r from the planet is

$\dot{M}_p = 4\pi r^2 \rho(r) v(r)$ where $\rho(r)$ and $v(r)$ are the the wind’s mass density and speed. Under the simplifying assumption that the wind is *isothermal*, the wind speed equals the sound speed c_s at the critical point distance $r_s = GM_p/(2c_s^2)$; in this case the crtical point occurs at the sonic point. The isothermal sound speed is $c_s = (\mathcal{R}T/\mu)^{1/2}$ where \mathcal{R} is the gas constant and μ is the mean weight per particle (amu) in the wind. For a pure neutral hydrogen atmosphere $\mu = 1$ and if fully ionized $\mu = 0.5$. Even though simulations of hot Jupiter atmospheres indicate the wind is not strictly isothermal (e.g Salz et al. 2016), the isothermal approximation is still useful as a gauge of the mass loss rate, especially in view of all the other uncertainties involved such as atmospheric abundances.

Denoting the mass density at the sonic point as ρ_s gives the normalized mass loss rate in the isothermal approximation

$$\dot{M}_{p,s} \sim 10^{-9} \left[\frac{r_s}{10 R_J} \right]^2 \left[\frac{\rho_s}{10^{-15} \text{ g cm}^{-3}} \right] \left[\frac{c_s}{10 \text{ km s}^{-1}} \right] \quad (\text{M}_J \text{ yr}^{-1}). \quad (7)$$

Although the flux F_{XUV} incident on the planet does not appear explicitly in the above, it enters implicitly since it affects the temperature profile $T(r)$ via heat deposition and the quantities which determine the mass loss rate are temperature dependent. Detailed atmospheric radiative transfer modeling taking both heating and cooling into account are needed to reconstruct $T(r)$. Hydrodynamic models for hot Jupiters orbiting TTS with strong XUV emission predict that the atmospheric temperature will increase rapidly from a base level T_0 to a maximum value T_{max} and then slowly decline outward (Penz et al. 2008; MC09; Salz et al. 2016; Shaikhislamov et al. 2014). The maximum temperature is expected to self-regulate or “thermostat” at $T_{max} \sim 10,000$ K as a result of XUV heating being offset by radiative and adiabatic cooling. However, recent observations of the hot Jupiter WASP-189b suggest somewhat higher temperatures are possible (Sreejith et al. 2023). The base temperature T_0 can be approximated by the planet’s equilibrium temperature T_{eq} . Adopting an effective temperature $T_{eff,*} = 4620$ K for TAP 26 (Yu17) gives $T_{eq} = 760$ K for TAP 26 b, assuming a Bond albedo $A_B \approx 0.05 - 0.1$ (Sudarsky et al. 2000) with heat evenly distributed over the planet’s surface. Simulations of hot Jupiter atmospheres typically predict the flow to become supersonic at $r_s \approx 3 - 5 R_p$ (MC09; Owen & Adams 2014; Salz et al. 2016). At the sonic point the temperature is predicted to be a few thousand K. At $T \sim 2,000 - 4,000$ K the sound speed in neutral H gas is $c_s = 4 - 6 \text{ km s}^{-1}$.

In order to calculate the XUV heating rate (eqs. [4], [6]) the number density n_H is needed, and it varies with height in the planet’s atmosphere. Hot Jupiter models usually assume a base level density (or pressure) and extrapolate it outward. The base level density (or pressure) is quite uncertain and its uncertainty propagates into the derived mass loss rate (Shaikhislamov et al. 2014; Salz et al. 2016). Hot Jupiter simulations predict a typical number density at the sonic point $n_{H,s} \sim 10^6 - 10^7 \text{ cm}^{-3}$, or an equivalent neutral hydrogen mass density $\rho_s = \mu m_H n_{H,s} \sim 10^{-18} - 10^{-17} \text{ g cm}^{-3}$. Conversion of number to mass density requires knowledge of the atmsphere’s chemical composition which is generally not well-known and can vary with height, but observational constraints have been obtained for a few objects (e.g. Charbonneau et al. 2002; Cody & Sasselov 2002; see also the review of Fortney et al. 2021).

Using the above density estimates as a guide in eq. (7) and assuming $M_p \approx 2 M_J$ (Yu17) and radius $R_p \approx 1.3 R_J$ (Sarkis et al. 2021) for TAP 26 b, the inferred mass loss rate is $\dot{M}_p \lesssim 10^{-11} M_J \text{ yr}^{-1}$. Previous studies of late-type stars predict that most of the exoplanet’s photoevaporative mass-loss will occur during the first Gyr (Jackson et al. 2012). If the mas-loss rate of TAP 26 b

is set equal to the above upper limit and assumed to be constant over time, the hot Jupiter would shed less than 1% of its mass during the first Gyr of its life. This conclusion is strengthened when taking into account that the star’s XUV flux will decline with age (Güdel et al. 1997) along with the XUV-driven mass loss rate.

For comparison with the above, the energy-limited mass-loss rate is (Sanz-Forcada et al. 2011) $\dot{M}_{p,el} = 3F_{XUV}/(4G\rho_p\mathcal{K})$ where ρ_p is the planet’s mean mass density, $0 < \mathcal{K} \leq 1$ accounts for Roche lobe effects, G is the gravitational constant and F_{XUV} is the XUV flux at the planet’s surface. Assuming Roche lobe effects are negligible ($\mathcal{K} \approx 1$; Erkaev et al. 2007; Lammer et al. 2009) and normalizing to Jupiter’s mass density $\rho_J = 1.3 \text{ g cm}^{-3}$ gives $\dot{M}_{p,el} \sim 10^{-16}(\rho_p/\rho_J)^{-1}F_{XUV} \text{ (M}_J \text{ yr}^{-1})$. Expressing unattenuated high-energy flux F_{XUV} in terms of the star’s XUV luminosity $L_{XUV} = L_x + L_{EUV}$ and normalizing gives

$$\dot{M}_{p,el} \approx 5 \times 10^{-12} \left[\frac{\rho_p}{\rho_J} \right]^{-1} \left[\frac{a}{0.1 \text{ au}} \right]^{-2} \left[\frac{L_{XUV}}{10^{30} \text{ erg s}^{-1}} \right] \text{ (M}_{\text{Jup}} \text{ yr}^{-1}). \quad (8)$$

Adopting $L_x = 10^{30} \text{ erg s}^{-1}$ for TAP 26 and assuming $L_{EUV} \sim L_x$ yields $\dot{M}_{p,el} \sim 10^{-11}(\rho_p/\rho_J)^{-1} \text{ M}_J \text{ yr}^{-1}$. This energy-limited mass-loss rate is the same order of magnitude as the upper limit estimated above using the hydrodynamic approach but is subject to the aforementioned uncertainty in L_{EUV} .

The above estimates do not include the effects on mass loss due to any planetary magnetic field. The degree to which the planet’s wind is controlled by the B-field depends on the ratio of the wind’s ram pressure to the magnetic pressure and a modest field strength $B_p \sim 0.3 \text{ G}$ can lead to a significant reduction in \dot{M}_p (Owen & Adams 2014).

4.5. Comparison with V830 Tau

The solar-mass weak-lined TTS V830 Tau is remarkably similar to TAP 26 and may also host a close-in hot Jupiter V830 Tau b (Donati et al. 2015, 2016, 2017). But an attempt to confirm the radial velocity (RV) detection of the planet by Damasso et al (2020) yielded negative results so the planet’s existence needs confirmation. The RV data yielded an orbital period $P_{orb} = 4.927 \text{ d}$ and separation $a = 0.057 \text{ au}$, placing V830 Tau b in a tighter orbit than TAP 26 b. The K7-type host star V830 Tau has an estimated age of 2.2 Myr (Donati et al. 2015) and a 2.74 d rotation period (Grankin et al. 2008). It may thus be a younger but more slowly rotating analog of TAP 26, as discussed by Yu17.

Chandra observations of V830 Tau revealed variable X-ray emission with $\log L_x = 30.1 - 30.4 \text{ erg s}^{-1}$ (Skinner & Güdel 2021). But XMM-Newton observations recorded brighter flare emission up to $\log L_x = 30.87 \text{ erg s}^{-1}$ (Francosini et al. 2007, adjusted to $d = 130.4 \text{ pc}$). The lower end of the V830 Tau range overlaps that of TAP 26 but during flares V830 Tau is much more luminous than observed so far for TAP 26. Since X-ray time monitoring is still quite limited for both stars the full range of X-ray variability may not yet be sampled. At their young ages the Tu et al. (2015) evolutionary tracks place V830 Tau in the X-ray saturation regime and TAP 26 also in or near saturation. The mean hardness ratio $H.R = 0.36$ and median photon energy $E_{50} = 1.60 \text{ keV}$ of V830 Tau are greater than TAP 26 (Table 2) even though both stars have similar A_V . Thus, V830 Tau is characterized by hotter X-ray plasma. Also, the putative hot Jupiter orbiting V830 Tau lies at a separation $a = 0.057 \text{ au}$, half that of TAP 26 b. Thus, the unattenuated X-ray flux at V830 Tau b is at least four times greater than that at TAP 26 b.

5. SUMMARY

1. New observations of TAP 26 reveal a variable X-ray source whose X-ray flux and temperature changed over a few hours with temperature of the hotter plasma increasing to $kT_x \approx 4$ keV. Slower variability is also present. The X-ray flux range measured by Chandra brackets the flux measured previously by the Einstein Observatory. The Chandra X-ray luminosity is in the range $\log L_x(0.3-8 \text{ keV}) = 29.80 - 30.20 \text{ ergs s}^{-1}$.
2. Since the elevated X-ray emission detected on 1 Dec. 2021 was not present five days later at about the same rotation phase, the high X-ray state is evidently not tied to stellar rotation. Time coverage is not yet sufficient to determine whether the slower X-ray variability is modulated at the planet's orbital period.
3. The unattenuated X-ray flux impinging on the planet is $F_{x,unatten}(0.3-8 \text{ keV}) = (2.4 - 6.0) \times 10^4 \text{ erg cm}^{-2} \text{ s}^{-1}$, or $\sim 10^6$ times greater than the Sun's X-ray flux at Jupiter. The X-ray heating rate of the planet's atmosphere is $\Gamma_x \sim 10^{-18} \text{ ergs s}^{-1} \text{ cm}^{-3} n_{\text{H}}^{-1}$ where the H-nucleus number density n_{H} at the atmospheric height corresponding to $\tau_x=1$ is model-dependent and unspecified.
4. A comparison of TAP 26 b with previous studies of other hot Jupiters indicates that photoevaporative mass loss will be negligible over the first Gyr of the planet's life.

Support for this work was provided by Chandra award number GO2-23009X issued by the Chandra X-ray Center, which is operated by the Smithsonian Astrophysical Observatory (SAO) for and on behalf of NASA. This work has utilized HEASOFT developed and maintained by HEASARC at NASA GSFC.

This paper employs a list of *Chandra* datasets obtained by the Chandra X-ray Observatory contained in [DOI: 10.25574/cdc.218](https://doi.org/10.25574/cdc.218).

Facilities: CXO

Software: CIAO (Fruscione et al. 2006), XSPEC (Arnaud 1996)

REFERENCES

- Anders, E., & Grevesse, N. 1989, *GeoCoA*, 53, 197
- Arnaud, K.A. 1996, in *ASP Conf. Series* vol. 101, *Astronomical Data Analysis Software and Systems V*, ed. G. Jacoby & J. Barnes (San Francisco, CA; ASP), 17
- Bruderer, S., Doty, S.D., & Benz, A.O. 2009, *ApJS*, 183, 179
- Charbonneau, D., Brown, T.M., Noyes, R.W., & Gilliland, R.L. 2002, *ApJ*, 568, 377
- Cody, A.M. & Sasselov, D.D. 2002, *ApJ*, 569, 451
- Damasso, M., Lanza, A.F., Benatti, S. et al. 2020, *A&A*, 642, A133
- Dawson, R.I. & Johnson, J.A. 2018, *ARA&A*, 56, 175
- Donati, J.-F., Hébrard, E., Hussain, G.A.J. et al. 2015, *MNRAS*, 453, 3706
- Donati, J.-F., Moutou, C., Malo, L. et al. 2016, *Nature*, 534, 662
- Donati, J.-F., Yu, L., Moutou, C. et al. 2017, *MNRAS*, 465, 3343
- Erkaev, N.V. et al. 2007, *A&A*, 472, 329
- Feigelson, E.D., Jackson, J.M., Mathieu, R.D., Myers, P.C., & Walter, F.M. 1987, *AJ*, 94, 1251
- Fortney, J.J., Dawson, R.I., & Komacek, T.D. 2021, *JGR Planets*, 126, 2020JE006629
- Franciosini, E., Pillitteri, I., Stelzer, B. et al. 2007, *A&A*, 468, 485
- Fruscione, A., McDowell, J.C., Allen, G.E. et al. 2006, *Proc. SPIE*, 6270, 62701V
- Gorenstein, P., 1975, *ApJ*, 198, 95
- Grankin, K.N. 2013, *Astron. Lett.*, 39, 251
- Grankin, K.N., Bouvier, J., Herbst, W., & Melnikov, S.Y. 2008, *A&A*, 479, 827
- Güdel, M., Guinan, E.F., & Skinner, S.L. 1997, *ApJ*, 483, 947
- Haffert, S.Y., Bohn, A.J., de Boer, J., Snellen, I.A.G., Brinchmann, J., Girard, J.H., Keller, C.U., & Bacon, R. 2019, *Nature Ast.*, 3, 749
- Hecceg, G.J. & Hillenbrand, L.A. 2014, *ApJ*, 786, 97
- Igea, J. & Glassgold, A.E. 1999, *ApJ*, 518, 848
- Jackson, A.P., Davis, T.A., & Wheatley, P.J. 2012, *MNRAS*, 422, 2024
- Keppler, M., Benisty, M., Müller, A. et al. 2018, *A&A*, 617, A44
- Keppler, M., Teague, R., Bae, J. et al. 2019, *A&A*, 625, A118
- Lammer, H., Odert, P., Leitzinger, M. et al. 2009, *A&A*, 506, 399
- Morrison, R. & McCammon, D. 1983, *ApJ*, 270, 119
- Murray-Clay, R.A., Chiang, E.I., & Murray, N. 2009, *ApJ*, 693, 23 (MC09)
- Neuhäuser, R. Sterzik, M.F., Schmitt, J.H.M.M., Wichmann, R., & Krautter, J. 1995, *A&A*, 297, 391
- Owen, J.E. & Adams, F.C. 2014, *MNRAS*, 444, 3761
- Owen, J.E. & Jackson, A.P. 2012, *MNRAS*, 425, 2931
- Parker, E.N. 1958, *ApJ*, 128, 664
- Parker, E.N. 1965, *SSRv*, 4, 666
- Penz, T. et al. 2008, *Planetary and Sp. Science*, 56, 1260
- Ribas, I., Guinan, E.F., Güdel, M., & Audard, M. 2005, *ApJ*, 622, 680
- Salz, M., Czesla, S., Schneider, P.C., & Schmitt, J.H.M.M. 2016, *A&A*, 586, A75
- Sanz-Forcada, J., Micela, G., Ribas, I. et al. 2011, *A&A*, 532, A6
- Sarkis, P., Mordasini, C., Henning, Th., Marleau, G.D., & Mollière, P. 2021, *A&A*, 645, A79
- Shaikhislamov, I.F., Khodachenko, M.L., Sasunov, Y.L. Lammer, H. Kislyakova, K.G., & Erkaev, N.V. 2014, *ApJ*, 795, 132
- Shang, H., Glassgold, A.E., Shu, F.H., & Lizano, S. 2002, *ApJ*, 564, 853
- Skinner, S.L. & Audard, M. 2022, *ApJ*, 938, 134
- Skinner, S.L. & Güdel, M. 2021, *ApJ*, 920, 22
- Sreejith, A.G., France, K., Fossati, L. et al. 2023, *ApJL*, 954, L23
- Sudarsky, D., Burrows, A., & Pinto, P. 2000, *ApJ*, 538, 885
- Telleschi, A., Güdel, M., Briggs, K.R., Audard, M., & Palla, F. 2007, *A&A*, 468, 425
- Tu, L., Johnstone, C.P., Güdel, M., & Lammer, H. 2015, *A&A*, 577, L3
- Vuong, M.H., Montmerle, T., Grosso, N., Feigelson, E.D., Verstraete, L., & Ozawa, H., 2003, *A&A*, 408, 581
- Yelle, R.V. 2004, *Icarus*, 170, 167
- Yu, L., Donati, J.-F., Hébrard, E.M. et al. 2017, *MNRAS*, 467, 1342 (Yu17)